Text S1. Performance check of the DMAs

Before and after the atmospheric observation, the accuracy of the sizing by three DMAs was assessed using standard size PSL particles (JSR SIZE STANDARD PARTICLES: SC-0055-D, SC-0100-D, and SC-032-S; Thermo Scientific^{TM}: 3500A). The mode diameters from fittings for the measurement data (Kawana et al., 2014) were compared with the manufacturer warranty (Table S1), which is interpreted as prescribed ranges of mean diameter ± the expanded uncertainty (k = 2). The mode diameters after the atmospheric observation agreed with those before the observation within 0.84 %. The results obtained before the atmospheric observation are as follows. For DMA1, whereas the measured mode diameter of SC-0100-D was within the prescribed range, the measured mode diameters of SC-0055-D and SC-032-S were 1.0 % larger than the upper end of the prescribed range and 0.76 % lower than the lower end of the prescribed range, respectively. For DMA2, the measured mode diameter of SC-0055-D was 1.5 % larger than the upper end of the prescribed range, and the measured mode diameters of SC-0100-D, SC-032-S, and 3500A were 0.85, 3.2, and 2.2 % lower than the lower end of the prescribed ranges, respectively. For DMA3, the measured mode diameter of SC-0055-D was 6.9 % larger than the upper end of the prescribed diameter range, and the measured mode diameters for all three of the other PSL standards were within the prescribed ranges.

Text S2. Performance check of HTDMA using ammonium sulfate particles

Before the atmospheric observation, an aqueous solution of ammonium sulfate (AS) (99.999 % purity, Sigma-Aldrich) was nebulized and the generated aerosols were dried and introduced to the HTDMA to assess the difference in the sizing between the two DMAs under dry condition and to validate the control of RH in the HTDMA. The diameter setting for the measurements was the same as that of ambient particles (Sect. 2). The mean growth factors ($g_{f,m}$) of the AS particles under both dry and wet conditions were

retrieved using the same method as that for ambient particles (Sect. 3.1). The $g_{f,m}$ of the dry AS aerosol particles with diameters of 30–360 nm were 1.2–4.1 % deviated from unity (Table S2). The deviations were used to correct the difference of sizing between DMA1 and DMA2 for the g_f of AS and ambient aerosol particles measured at 85 % RH. The respective $g_{f,m}$ of AS particles at 85 % RH with d_{dry} of 30, 50, 70, 100, 200, 300, and 360 nm were 1.52, 1.54, 1.54, 1.54, 1.55, 1.57, and 1.59, which agree within 2.0 % with the calculated values ($g_{f,AS}$; Table S2) based on the Extended AIM Aerosol Thermodynamics Model II (E-AIM II, http://www.aim.env.uea.ac.uk/aim/model2/model2a.php; Clegg et al., 1998; Wexler and Clegg, 2002). The derivation of the hygroscopic growth factor of AS particles using the E-AIM II model is presented in Text S6.

Text S3. PMF analysis of organic mass spectra

The bulk mass spectra of organics observed in V-mode were subjected to PMF analysis (PMF Evaluation Tool v3.04A). For the analysis, high resolution fragment ions with signal to noise ratio (SNR) smaller than 0.2 were omitted, fragments with SNR in the range of 0.2–2 were down-weighted by a factor of three, and fragments related to CO2 (i.e., CO2, CO, H2O, HO, and O) were down-weighted so that fragment CO2 only contributed once. The obtained two-factor solution, with a more-oxygenated OA component (MOOA) and a less-oxygenated OA component (LOOA), with seed = 1 and fpeak = 0, was adopted for the explanation of OA composition. The two-factor PMF results are summarized in Fig. S1.

Text S4. Data screening methods

All the data except for the meteorological data obtained during the atmospheric observation were subjected to the screening to exclude data under possible influence from intermittent local anthropogenic emissions. For the SMPS data with 5 min resolution, and the BC and gaseous species data with 30 min resolution, if

the data value at one point was more than 30 % deviated from both the former data point and the next data point in the time series, the data at that time point was deleted. The chemical composition data derived from AMS measurements with 30 min resolution were deleted whenever the BC data were deleted. The hygroscopic growth data derived from the HTDMA measurements were deleted whenever the SMPS data were deleted. Furthermore, if the total count of particles measured using the CPC in the HTDMA in the diameter range of 0.80–2.2 times of d_{dry} (or 0.80–2.0 times of d_{dry} for particles with d_{dry} of 360 nm) during a single scan was less than eight, the HTDMA data was not used, either. Here, the d_{dry} were corrected for the difference of sizing between DMA1 and DMA2.

Text S5. Derivation of size-resolved volume fractions of the chemical components

The size-resolved volume fractions of inorganic salts (ε_i), organics (ε_{org}), and BC (ε_{BC}) were calculated as follows. First, BC was assumed to be internally mixed with non-refractory aerosol components and to have the same mass-size distribution as OA. The aerosol particles were assumed to be spherical and without voids. Using the PToF mode data from the AMS, the mass concentrations of aerosol components in the vacuum aerodynamic diameter (d_{va}) ranges that are ~1.0 (0.98–0.99) to 2.0 times of d_{dry} were obtained: the ranges of d_{va} for particles with d_{dry} of 100, 200, 300, and 360 nm were 98–197, 197–395, 295–589, and 353–707 nm, respectively. Second, the mole amounts of sulfate, nitrate, and ammonium in 1 m^3 of air were derived. Third, the amount of ammonium nitrate (AN), ammonium sulfate (AS), letovicite (LET), ammonium hydrogen sulfate (AHS), and sulfuric acid (SA) per mole in 1 m^3 of air was determined, assuming that nitrate was fully neutralized with ammonium, and that sulfate could present in the form of AS, LET, AHS, and/or SA according to the amount of remaining ammonium. The detected non-refractory chloride was not considered because of its low concentration compared with the concentrations of the other non-refractory components. The contribution of sea salt and minerals to the sub-micrometer aerosol

particles was likely small (Han et al., 2014; Deng et al., 2018) and was also not considered. Fourth, the volumes of BC, OA, and LET were derived using their respective densities and the volumes of AN, AS, AHS, and SA were derived using their respective molar volumes. The density of BC was assumed to be 1.77 g cm^{-3} (Park et al., 2004). The density of organics (ρ_{org}) was estimated to be 1.32 ± 0.09 g cm^{-3} using the O:C and H:C ratios of organics derived from AMS measurements (Kuwata et al., 2012), and the mean value of 1.32 g cm^{-3} was adopted for this study. The density of LET was assumed to be 1.83 g cm^{-3} (Padró et al., 2010). The molar volumes of AN, AS, AHS, and pure liquid SA, which are the same as the ones used in the E-AIM II model, were adopted in this study. Finally, the volume fractions of each species were obtained.

Text S6. Derivation of $g_{f,AS}$ and κ_i using the E-AIM II model

The hygroscopic growth factor of pure ammonium sulfate particles ($g_{f,AS}$) and the hygroscopicity parameter of each inorganic salt (κ_i) at 85 % RH were derived based on the output of the E-AIM II model and the κ–Köhler equation (Petters and Kreidenweis, 2007) as follows.

The water activity (a_w) range from 0.8000 to 0.8499 at a resolution of 0.0001 was applied to the E-AIM II model for unit mole of each inorganic salt at the temperature of 294 K. For the calculation, the partition of HNO_3, NH_3, and H_2SO_4 into the vapor phase was prevented and the formation of solid AS was also prevented. The hygroscopic growth factor (g_f) corresponding to each a_w was derived from the ratio of total wet volume (V_{wet}) to the dry molar volume of the pure salt. The κ_i corresponding to each a_w was derived from Equation 2 of Petters and Kreidenweis (2007). The exponential part of the κ–Köhler equation was derived on the assumption that the partial molar volume of water equals the molar volume of pure water. Here, a_w was calculated based on the relationship that the RH above the particle surface equals the product of the a_w and the exponential part of the κ–Köhler equation representing the Kelvin effect. For particles

with respective d_{dry}, an a_w value at which the RH above the particle surface was nearest to 85 % ($a_{w,85}$) was obtained by applying a wet diameter represented by the product of d_{dry} and g_f. The hygroscopicity parameter value at $a_{w,85}$ was defined as κ_i (Table S3). For AS, the g_f at $a_{w,85}$ was defined as $g_{f,AS}$ (Table S2). For the derivation of κ_i, the surface tension of the solution was applied, whereas for the derivation of κ_t (Sect. 3.1) the surface tension of pure water was applied. The uncertainty of the surface tension should not introduce large uncertainty in the derived κ_{org} because the difference of κ_i obtained using the surface tension of pure water and that obtained using the surface tension of the solution was small (within 0.38 %, Table S3).

Text S7. Determination of the range of d_{va} for the calculation of κ_{org}

The PToF mode AMS data over a lower d_{va} range was subjected to low signal intensity (Fig. S2) when it was adopted for the derivation of size-resolved κ_{org}. To determine the applicable range of d_{va} for this study, the mean mass-size distribution data of OA during the entire study period was compared to that of a baseline region (Fig. S3). The baseline region here is the transition region between the regions dominated by gaseous species and particle signals of OA, and corresponds to the PToF time region of 0.00135458–0.00150458 s. To eliminate data under the strong influence of the signals from gaseous species, the d_{va} of 98 nm (where the mass ratio of the mean observed OA to mean baseline OA became greater than three) was adopted as the lower limit of the d_{va} range for the deviation of κ_{org}. In Fig. S3, the mean mass-size distribution of OA for filtered air (collected by connecting a HEPA filter (TSI) to the inlet tubing outside the instrument room) is also presented for comparison. Only in the d_{va} range of 90–716 nm, the mean values of the observed OA mass in each d_{va} bin were greater than that of OA for the filtered air. This also indicates the strong influence of the signals from gaseous species at d_{va} smaller than ~90 nm. Because the OA data of filtered air was noisy, it was not used for the determination of the applicable d_{va} range.

Text S8. Derivation of size-resolved PMF factors

To explain the diurnal variation and size-dependence of κ_{org} from the compositional characteristics of OA, size-resolved PMF factors (LOOA and MOOA) were derived through multivariable linear regression analysis as follows.

First, the fragment profiles of LOOA and MOOA from bulk OA mass spectra were converted to the profiles in unit m/z resolution by summing up the intensity of the fragment ion signals at the same unit m/z. Then, for each time period in 2 h time resolution and for each PToF size bin *i*, the contributions from LOOA (a_i) and MOOA (b_i) were derived using the Solver function in Microsoft Excel by minimizing the value of the following formula:

$$\sum_{j=12}^{115} \left[x_{ij} - \left(a_i f_{1j} + b_i f_{2j}\right)\right]^2$$

Where x_{ij} is the measured signal intensity in size bin *i* at m/z = *j*, and f_{1j} and f_{2j} are the respective normalized signal intensity of LOOA and MOOA at m/z = *j*. The unit of x_{ij}, a_i, and b_i was μg m^{-3}, whereas f_{1j} and f_{2j} were dimensionless.

The size-resolved LOOA and MOOA were derived for the d_{va} range from ≤ 10 nm to around 900 nm (Fig. S6). However, only the d_{va} range above 98 nm was adopted for the analysis. This is because the uncertainty of the contributions from LOOA and MOOA in the lower d_{va} range was presumably relatively large, given the low organic signal intensity (Fig. S3) and high residual to measured OA mass ratio (Fig. S6).

Text S9. Assessment of the contributions of BSOA and anthropogenic OA to the enhancement of OA in the daytime

The contributions of BSOA and anthropogenic OA to the enhancement of OA in the daytime (in relation to the background period) were assessed using BC as a tracer of OA that did not come from BSOA

formation (non-BSOA-OA). Here, the non-BSOA-OA was considered the sum of regional OA and other anthropogenic OA. The diurnal variation data on the mass concentration of BC was scaled to represent the diurnal variation of non-BSOA-OA. For the scaling, the observed OA during the background period (i.e., 0600–0800 JST, when the daily minima of m_{org} appeared) was assumed to be composed only of non-BSOA-OA. The scaling factor was calculated to be 36.5. The mass concentrations of non-BSOA-OA ($m_{non\text{-}BSOA,bulk}$) and BSOA ($m_{BSOA,bulk}$) were then estimated using the following equations.

$$m_{non\text{-}BSOA,bulk} = m_{BC} \times 36.5 \quad \text{(S1)}$$

$$m_{BSOA,bulk} = m_{org} - m_{non\text{-}BSOA,bulk} \quad \text{(S2)}$$

Note that $m_{BSOA,bulk}$ and $m_{non\text{-}BSOA,bulk}$ are different from the mass concentrations of the BSOA and ROA defined from the size-resolved LOOA/MOOA data (Sect. 4.2.2 and Text S10). The $m_{BSOA,bulk}$ may be negatively biased because the charring of OA during the PSAP measurement may have resulted in a positive bias of m_{BC}. The increase of the OA mass concentration in the daytime ($m_{org,ENH}$) was estimated by subtracting the m_{org} during the background period from that during the period of interest. The ratio of $m_{BSOA,bulk}$ to $m_{org,ENH}$ was in the range 0.6–0.9 during 1200–1600 JST, and it was in the range 0.1–0.5 during 1600–2030 JST (Fig. S10). The result indicates that BSOA was the main contributor to the enhancement of OA at least during 1200–1600 JST. In a later period, a larger contribution from anthropogenic OA is not ruled out.

Text S10. Derivation of v_{BSOA} and v_{ROA} from v_{LOOA} and v_{MOOA}

Because the observed OA can be assumed to be contributed either by LOOA and MOOA, or by BSOA and ROA, the sum of LOOA and MOOA should equal the sum of BSOA and ROA. The size-resolved v_{BSOA} and v_{ROA} can be derived from the size-resolved v_{LOOA} and v_{MOOA}. From the analysis in Sect. 4.2.2, 0.97 (0.52), 0.88 (0.53), 0.80 (0.50), and 0.79 (0.45) of the volume of BSOA (ROA) for particles with d_{dry}

of 100, 200, 300, and 360 nm were assigned to LOOA, and the balances were assigned to MOOA. The relations are expressed by the equations:

$$v_{BSOA} + v_{ROA} = v_{LOOA} + v_{MOOA} \quad \text{(S3)}$$

$$a \times v_{BSOA} + b \times v_{ROA} = v_{LOOA} \quad \text{(S4)}$$

Where v_{BSOA}, v_{ROA}, v_{LOOA}, and v_{MOOA} are the size-resolved volume concentrations of BSOA, ROA, LOOA, and MOOA, respectively, and a and b represent the size-resolved volume fractions of BSOA and ROA, respectively, that were assigned to LOOA. The volume concentrations of BSOA and ROA were estimated using the equations:

$$v_{BSOA} = [(1 - b) / (a - b)] \times v_{LOOA} - [b / (a - b)] \times v_{MOOA} \quad \text{(S5)}$$

$$v_{ROA} = [(a - 1) / (a - b)] \times v_{MOOA} + [a / (a - b)] \times v_{LOOA} \quad \text{(S6)}$$

Equations (S5) and (S6) were used to estimate the contributions of BSOA to aerosol water uptake and to the CCN number concentration (Sect. 4.4 and Text S11).

Text S11. Estimation of the contributions of OA and BSOA to CCN concentrations

The contributions of OA and BSOA to the CCN number concentration were estimated from their size-resolved fractional contributions to aerosol water uptake and from the measured aerosol number-size distributions. The analysis was performed for diurnal variation data with 2 h resolution. A schematic of the estimate is presented in Fig. S17. For the estimate, the observed aerosol particles were assumed to be internally mixed, and all the particles with d_{dry} larger than 70 nm were assumed to be CCN active. The contributions of OA (BSOA) to the water uptake of particles with d_{dry} of 100, 200, 300, and 360 nm were applied for the diameter ranges of 70–150, 150–250, 250–330, 330–430 nm, respectively. For the diameter ranges larger than 430 nm, the CCN number concentration contributed by OA (BSOA) was not considered because of the low aerosol number concentrations. In each diameter range, the fractional contribution of

OA (BSOA) to $dN_{CN}/d\log d_{dry}$ equals the fractional contribution of OA (BSOA) to the total aerosol water uptake, which was represented as the product of the volume fraction of OA (BSOA) and κ_{org} (κ_{BSOA}) divided by κ_t [i.e., $\varepsilon_{org}\kappa_{org}/\kappa_t$ ($\varepsilon_{BSOA}\kappa_{BSOA}/\kappa_t$)]. The total fractional contribution of OA (BSOA) to the total CCN number concentration, $F_{CCN,OA}$ ($F_{CCN,BSOA}$), equals the integration of the product of the water uptake fraction and $dN_{CN}/d\log d_{dry}$ above the assumed CCN activation diameter (70 nm), divided by the total CCN number concentration.

For the above analysis, the water uptake of each aerosol component was represented by the product of the volume fraction of the aerosol component (ε_i) and its hygroscopicity (κ_i), that is, $\varepsilon_i\kappa_i$. The mean ε_i in each 2 h time section of the day was derived as follows. First, the mean values of the volume concentrations of each inorganic species, organics, and organic fractions (AN, AS, LET, AHS, SA, BC, OA, LOOA, and MOOA; $\bar{v}_i$) were calculated from the 2 h resolution data. Second, the mean volume concentrations of LOOA ($\bar{v}_{LOOA}$) and MOOA ($\bar{v}_{MOOA}$) were scaled so that their sum equals the mean volume concentration of OA ($\bar{v}_{OA}$). Third, the mean volume concentrations of BSOA ($\bar{v}_{BSOA}$) and ROA ($\bar{v}_{ROA}$) were estimated using Eqs. (S5) and (S6). Then, ε_i was calculated directly from those $\bar{v}_i$. The κ of the inorganic salts under the condition of 0.42 % SS, and at the temperature of the HTDMA measurement in this study, were used to consider the difference of κ between sub- and super-saturated water vapor conditions. Here, the κ for AN, AS, LET, AHS, and SA were calculated to be 0.73, 0.60, 0.63, 0.62, and 0.65, respectively, following the method in Deng et al. (2018). The difference of the κ of organics under sub- and super-saturated conditions was not considered. The κ values of OA and BSOA used for the calculation are presented in Tables S10 and S11, respectively. The contributions of OA and BSOA to the water uptake were calculated as $\varepsilon_{org}\kappa_{org}/\kappa_{t,reconst,org}$ and $\varepsilon_{BSOA}\kappa_{BSOA}/\kappa_{t,reconst,BSOA}$, respectively, where,

$$\kappa_{t,reconst,org} = \varepsilon_{AN}\kappa_{AN} + \varepsilon_{AS}\kappa_{AS} + \varepsilon_{LET}\kappa_{LET} + \varepsilon_{AHS}\kappa_{AHS} + \varepsilon_{SA}\kappa_{SA} + \varepsilon_{org}\kappa_{org} \quad (S7)$$

$$\kappa_{t,reconst,BSOA} = \varepsilon_{AN}\kappa_{AN} + \varepsilon_{AS}\kappa_{AS} + \varepsilon_{LET}\kappa_{LET} + \varepsilon_{AHS}\kappa_{AHS} + \varepsilon_{SA}\kappa_{SA} + \varepsilon_{BSOA}\kappa_{BSOA} + \varepsilon_{ROA}\kappa_{ROA}$$

(S8)

Text S12. Assessment of the change of CCN activation diameter accompanying the aging of BSOA

The aging of BSOA may change the CCN activation diameter and influence the prediction of $F_{CCN,BSOA}$. However, the change and the influence are considered to be small as explained below. If the range of κ_t of 0.17 to 0.35 (i.e., the κ_t range of (mean – SD) to (mean + SD) under 0.42 % SS condition in Deng et al. (2018)), and the approximate maximum ε_{BSOA} of 0.6 (Fig. S18) are applied, the increase of κ_{BSOA} by 0.09 (i.e., the difference between κ_{BSOA} and κ_{ROA} for particles with d_{dry} of 100 nm) leads to a decrease in the CCN activation diameter by 3–7 nm. The resulting decrease leads to increase of the predicted $F_{CCN,BSOA}$ by 0.41–3.8 %, which is regarded as small.

References:

Clegg, S. L., Brimblecombe, P., and Wexler, A. S.: Thermodynamic model of the system H+-NH4+-SO42−-NO3−-H2O at tropospheric temperatures, Journal of Physical Chemistry A, 102, 2137-2154, 10.1021/jp973042r, 1998.

Deng Y., Kagami S., Ogawa S., Kawana K., Nakayama T., Kubodera R., Adachi K., Hussein T., Miyazaki Y., and Mochida M.: Hygroscopicity of organic aerosols and their contributions to CCN concentrations over a mid-latitude forest in Japan, accepted for publication in Journal of Geophysical Research-Atmospheres, 10.1029/2017JD027292, 2018.

Draxier, R. R., and Hess, G. D.: An overview of the HYSPLIT_4 modelling system for trajectories, dispersion and deposition, Australian Meteorological Magazine, 47, 295-308, 1998.

Han, Y. M., Iwamoto, Y., Nakayama, T., Kawamura, K., and Mochida, M.: Formation and evolution of biogenic secondary organic aerosol over a forest site in Japan, Journal of Geophysical Research-Atmospheres, 119, 259-273, 10.1002/2013jd020390, 2014.

Kawana, K., Kuba, N., and Mochida, M.: Assessment of cloud condensation nucleus activation of urban aerosol particles with different hygroscopicity and the application to the cloud parcel model, Journal of Geophysical Research-Atmospheres, 119, 3352-3371, 10.1002/2013jd020827, 2014.

Kuwata, M., Zorn, S. R., and Martin, S. T.: Using Elemental Ratios to Predict the Density of Organic Material Composed of Carbon, Hydrogen, and Oxygen, Environmental Science & Technology, 46, 787-794, 10.1021/es202525q, 2012.

Padro, L. T., Tkacik, D., Lathem, T., Hennigan, C. J., Sullivan, A. P., Weber, R. J., Huey, L. G., and Nenes, A.: Investigation of cloud condensation nuclei properties and droplet growth kinetics of the water-

soluble aerosol fraction in Mexico City, Journal of Geophysical Research-Atmospheres, 115, 13, 10.1029/2009jd013195, 2010.

Park, K., Kittelson, D. B., Zachariah, M. R., and McMurry, P. H.: Measurement of inherent material density of nanoparticle agglomerates, Journal of Nanoparticle Research, 6, 267-272, 10.1023/B:NANO.0000034657.71309.e6, 2004.

Petters, M. D., and Kreidenweis, S. M.: A single parameter representation of hygroscopic growth and cloud condensation nucleus activity, Atmospheric Chemistry and Physics, 7, 1961-1971, 10.5194/acp-7-1961-2007, 2007.

Wexler, A. S., and Clegg, S. L.: Atmospheric aerosol models for systems including the ions H+, NH4+, Na+, SO42−, NO3−,Cl−, Br−, and H2O, Journal of Geophysical Research-Atmospheres, 107, 14, 10.1029/2001jd000451, 2002.

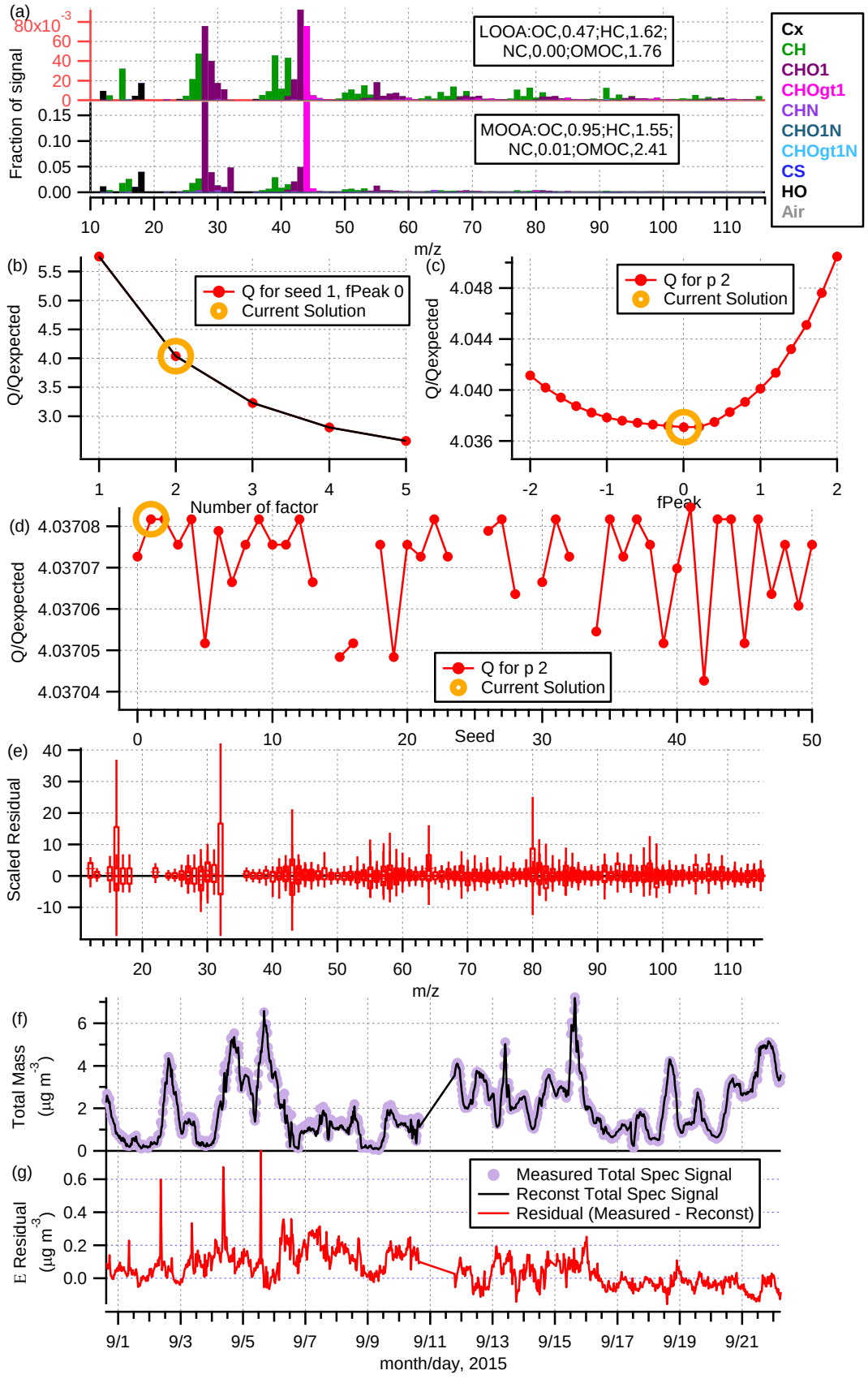
(a)
Fraction of signal
LOOA:OC,0.47;HC,1.62;
NC,0.00;OMOC,1.76
MOOA:OC,0.95;HC,1.55;
NC,0.01;OMOC,2.41
Cx
CH
CHO1
CHOgt1
CHN
CHO1N
CHOgt1N
CS
HO
Air
m/z
(b)
Q/Qexpected
Q for seed 1, fPeak 0
Current Solution
Number of factor
(c)
Q for p 2
Current Solution
fPeak
(d)
Q/Qexpected
Q for p 2
Current Solution
Seed
(e)
Scaled Residual
m/z
(f)
Total Mass (µg m-3)
(g)
E Residual (µg m-3)
Measured Total Spec Signal
Reconst Total Spec Signal
Residual (Measured - Reconst)
month/day, 2015

Figure S1: Summary of the two-factor result from the PMF analysis: (a) organic mass spectra of LOOA and MOOA colored according to ion groups (fpeak = 0 and SEED = 1), and the atomic ratios of O to C, H to C, and N to C, as well as OM to OC ratio for each factor; (b) Q/Qexpected as a function of the number of factors, where Q is the sum of the weighted squared residuals and Qexpected is the expected Q value; (c) Q/Qexpected as a function of the fpeak values with SEED = 1 and the number of factor = 2; (d) Q/Qexpected as a function of the SEED values with fpeak = 0 and the number of factor = 2; (e) distributions of the scaled residual for each m/z (fpeak = 0 and SEED = 1); time series of (f) the measured organic mass concentrations and those reconstructed (= LOOA + MOOA) (fpeak = 0 and SEED = 1), and (g) residual OA (= measured − reconstructed) (fpeak = 0 and SEED = 1).

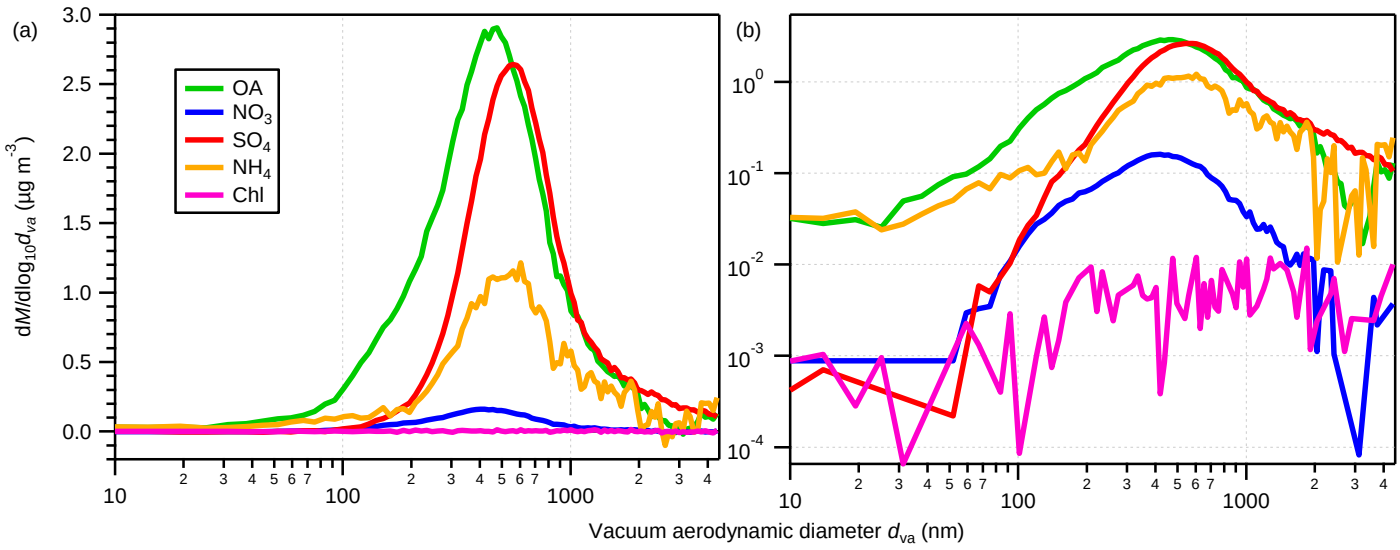

Figure S2: Mean mass-size distributions of organics (OA), sulfate (SO_4), ammonium (NH_4), nitrate (NO_3), and chloride (Chl) in (a) linear and (b) logarithmic scales over the entire study period.

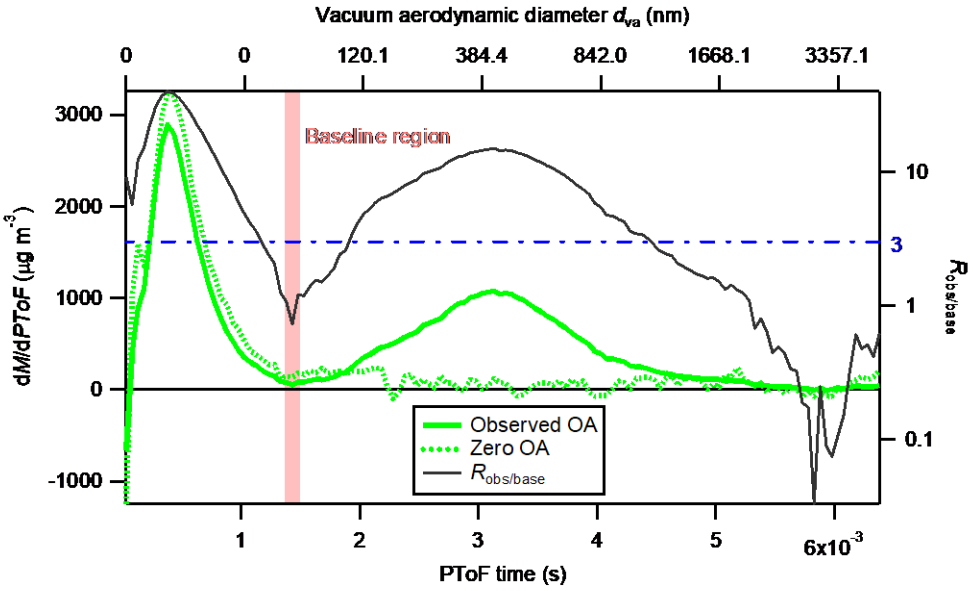

Figure S3: d*M*/d*PToF* (*M* and *PToF* here refer to mass concentration and PToF time, respectively) versus PToF time for the observed OA and OA measured by placing a HEPA filter in the inlet tubing outside the instrument room (zero OA), averaged for the entire study period. The region shaded in pink indicates the PToF time region chosen as a baseline for evaluation of the effective PToF diameter range. (Note that this is not the DC marker region.) The dark solid curve is the absolute value of the ratio of the observed OA at respective PToF time to the mean of the observed OA in the baseline region ($R_{obs/base}$). The blue dash-dotted line indicates the $R_{obs/base}$ value of three. The vacuum aerodynamic diameter that corresponds to the PToF time is presented on the top axis.

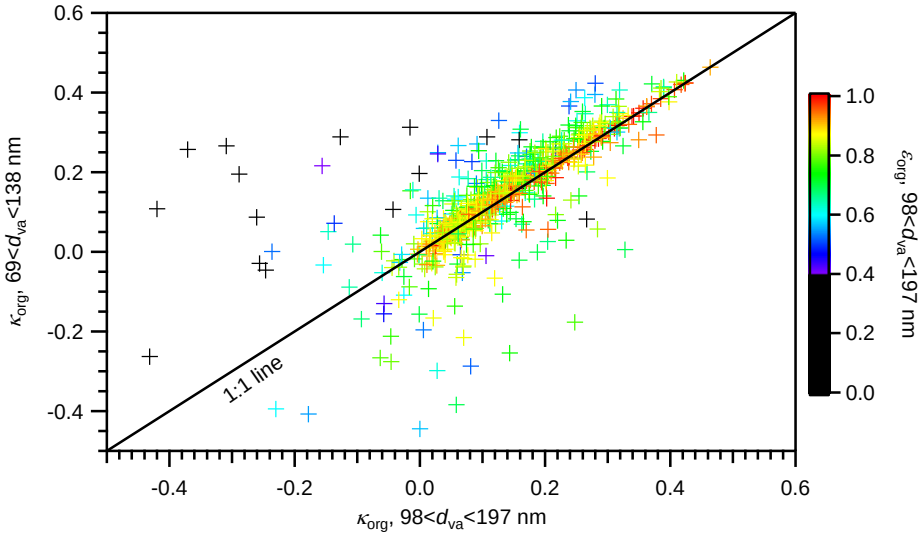

Figure S4: κ_{org} of 100 nm particles derived based on the chemical composition in the vacuum aerodynamic diameter (d_{va}) range of 69–138 nm versus that of 98–197 nm. Data points with κ_{org} smaller than −0.50 or κ_{org} higher than 0.60 are not presented.

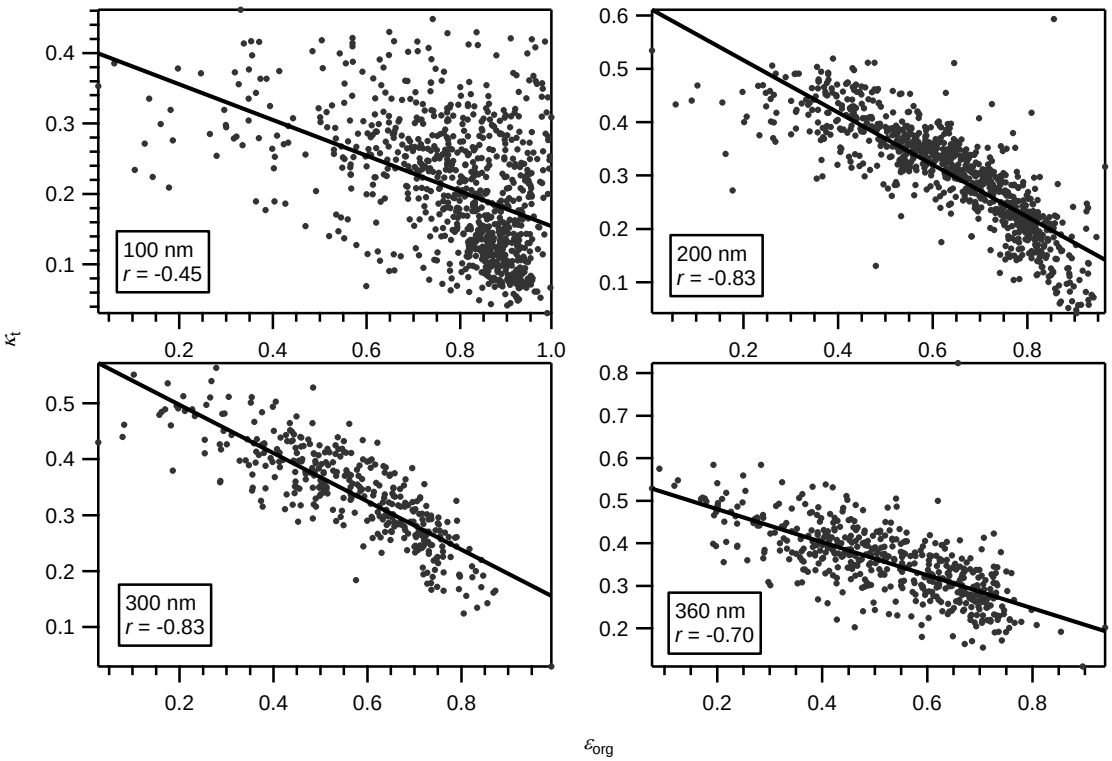

Figure S5: κ_t versus ε_{org} for particles with d_{dry} of 100, 200, 300, and 360 nm for the entire study period. In each panel, marks and a solid line represent individual data and the corresponding linear regression line, respectively. The correlation coefficient (r) of each is also presented.

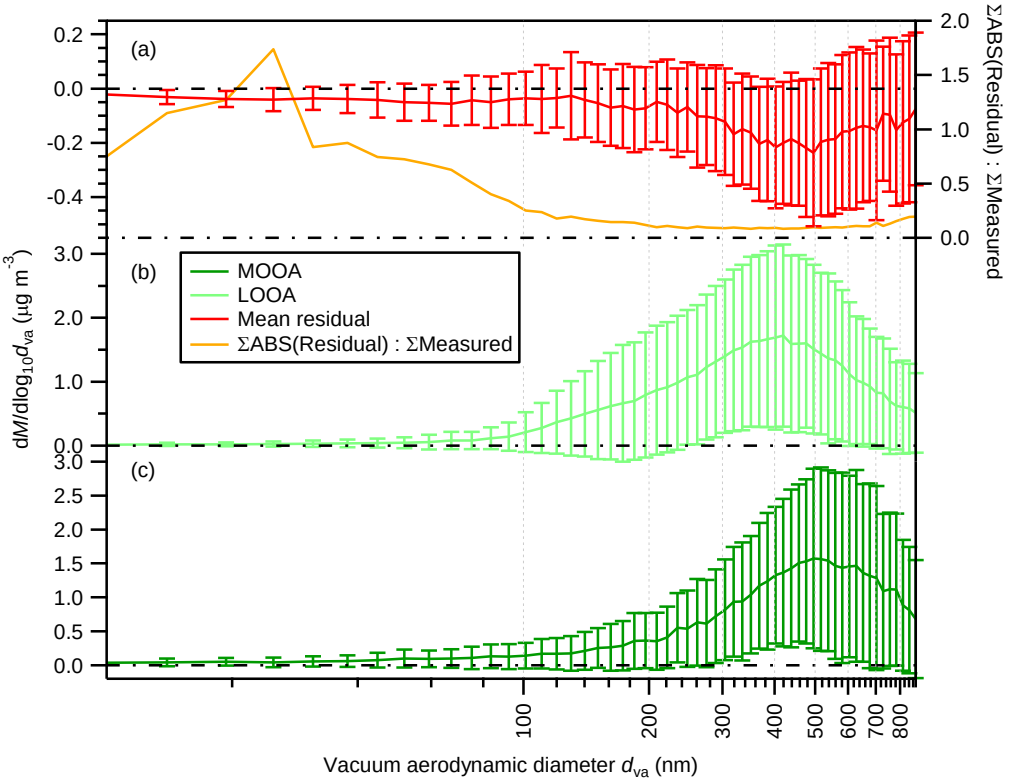

Figure S6: Mean mass-size distributions of (a) residual, (b) LOOA, and (c) MOOA over the entire study period. The residual is the difference between the measured and reconstructed (i.e., LOOA + MOOA) mass concentrations of OA in each size bin. The error bars indicate the standard deviation. The ratios of the sum of the absolute value of the residual to the measured mass concentration of OA are superimposed in panel (a) (right axis).

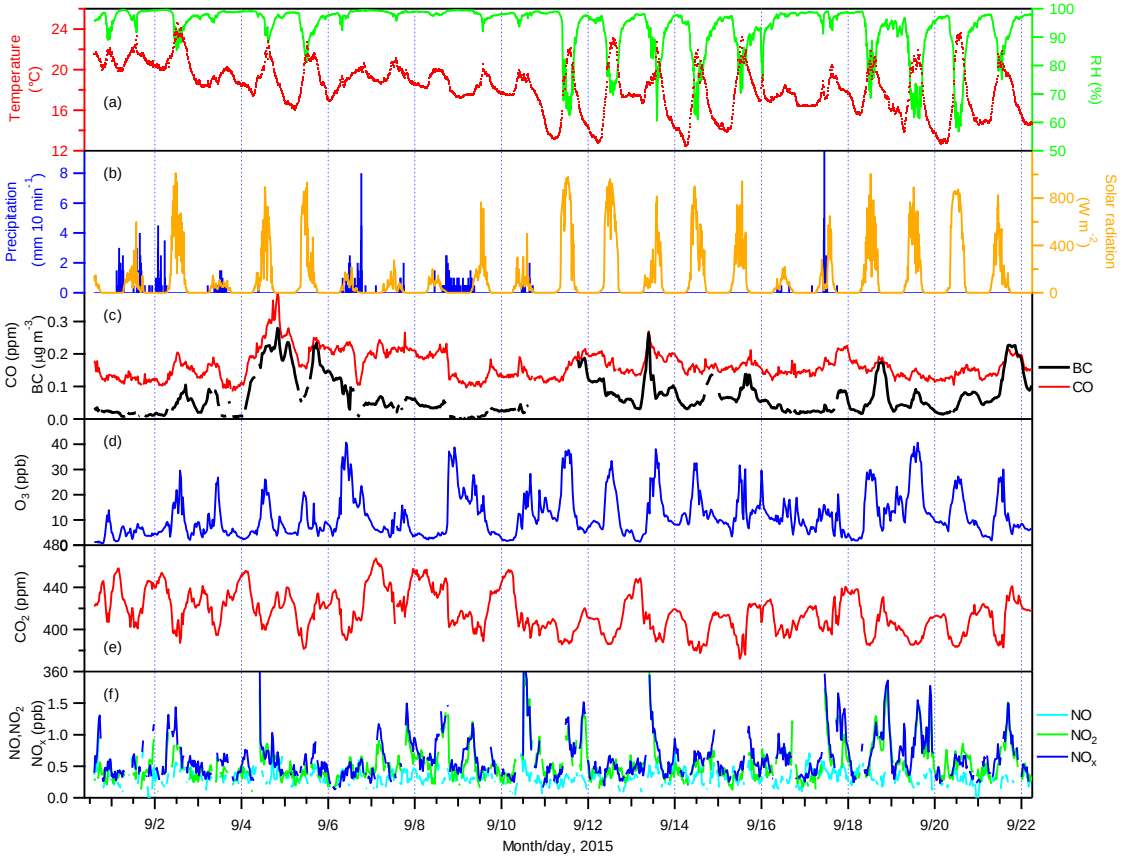

Figure S7: Time series of (a) air temperature and relative humidity (RH), (b) precipitation and solar radiation, (c) mass concentration of BC, and mixing ratios of (c) CO, (d) O_3, (e) CO_2, and (f) NO, NO_2, and NO_x.

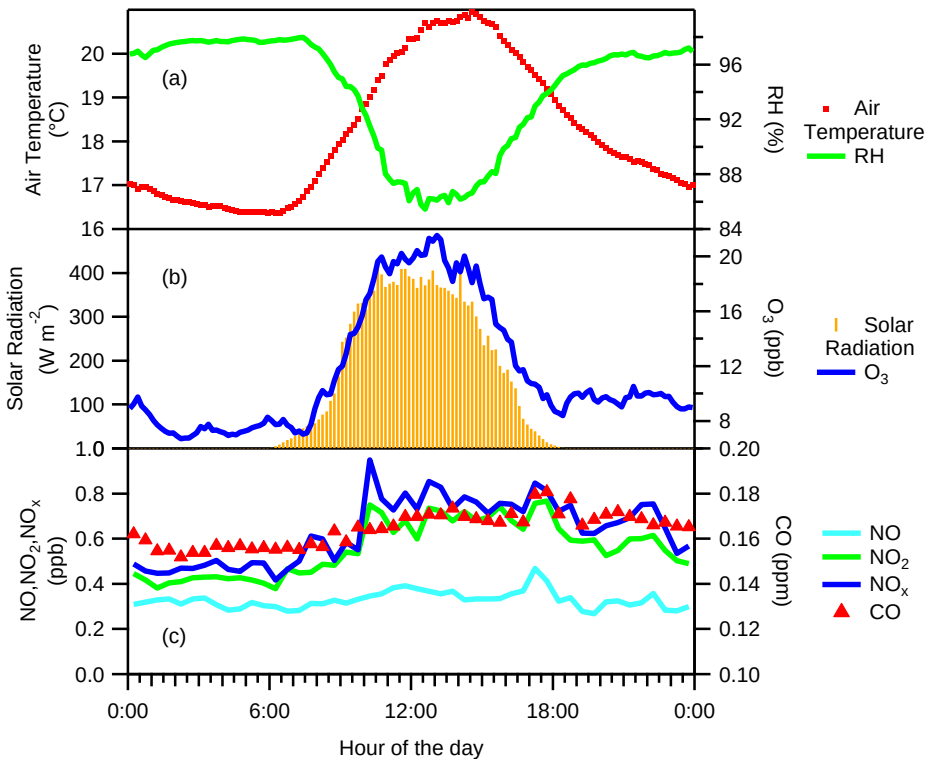

Figure S8: Diurnal variations of (a) air temperature and relative humidity (RH), (b) solar radiation and the mixing ratios of O_3, and (c) mixing ratios of NO, NO_2, NO_x, and CO over the entire study period.

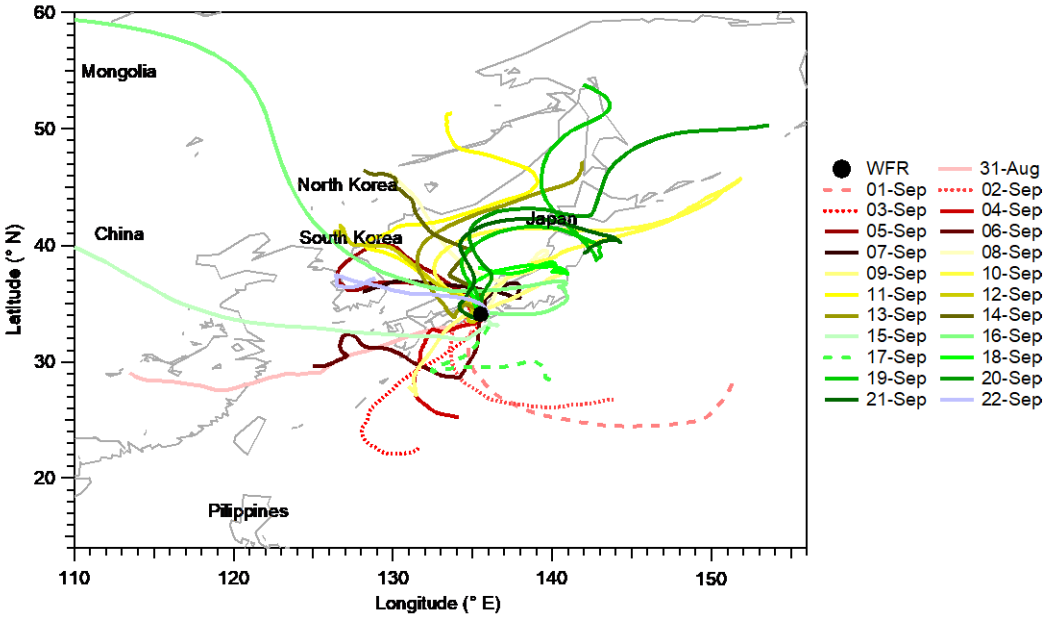

Figure S9: Five-day backward air mass trajectories from 500 m agl (above ground level) over Wakayama Forest Research Station at one-day intervals. The arrival time of the air masses at the study site was 1500 JST. The solid circle denotes the location of the study site. Solid trajectories are for days when more than 22 of the 24 hourly trajectories are from terrestrial regions. Dashed trajectories are for days when more

than 21 of the 24 hourly trajectories are from the North Pacific. Dotted trajectories are for days when 10 of the 24 hourly trajectories are from the North Pacific. The map is based on GSHHG 2.3.4; the shoreline polygon data at crude resolution is used. We consider an air mass is from the North Pacific if the trajectory never passes over terrestrial area that appears on the map before it reaches the Kii Peninsula. The trajectories were produced using NOAA's HYSPLIT atmospheric transport and dispersion modeling system (Draxler and Hess, 1998).

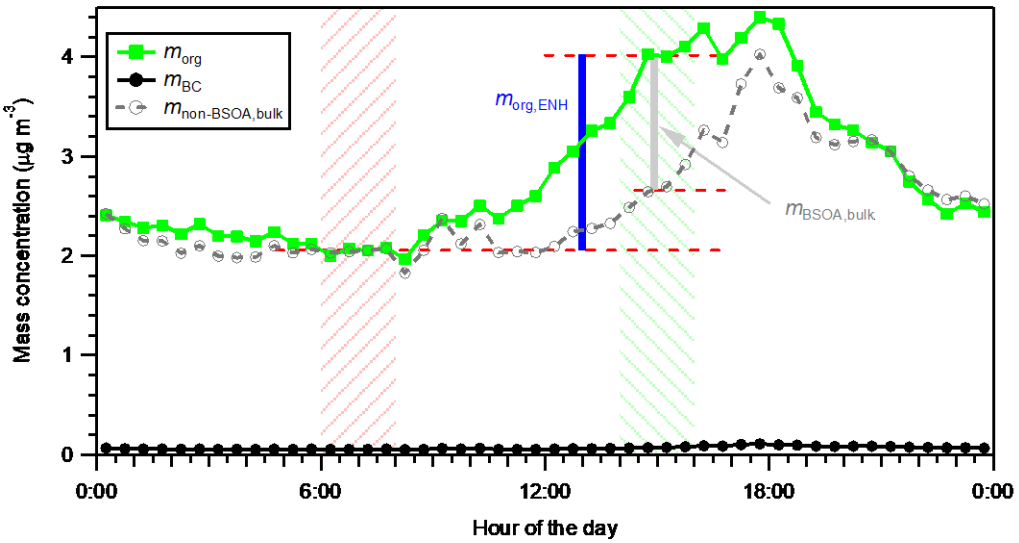

Figure S10. Diurnal variation of the mass concentrations of OA (m_{org}), BC (m_{BC}), and non-BSOA-OA ($m_{non\text{-}BSOA,bulk}$; Text S9) during the entire study period. The left-slash pattern represents the background period. As an example, the vertical bars represent the estimates of the total enhancement of OA ($m_{org,ENH}$; blue) and the enhancement contributed by BSOA ($m_{BSOA,bulk}$; gray) for the period 1400–1600 JST (right slash pattern).

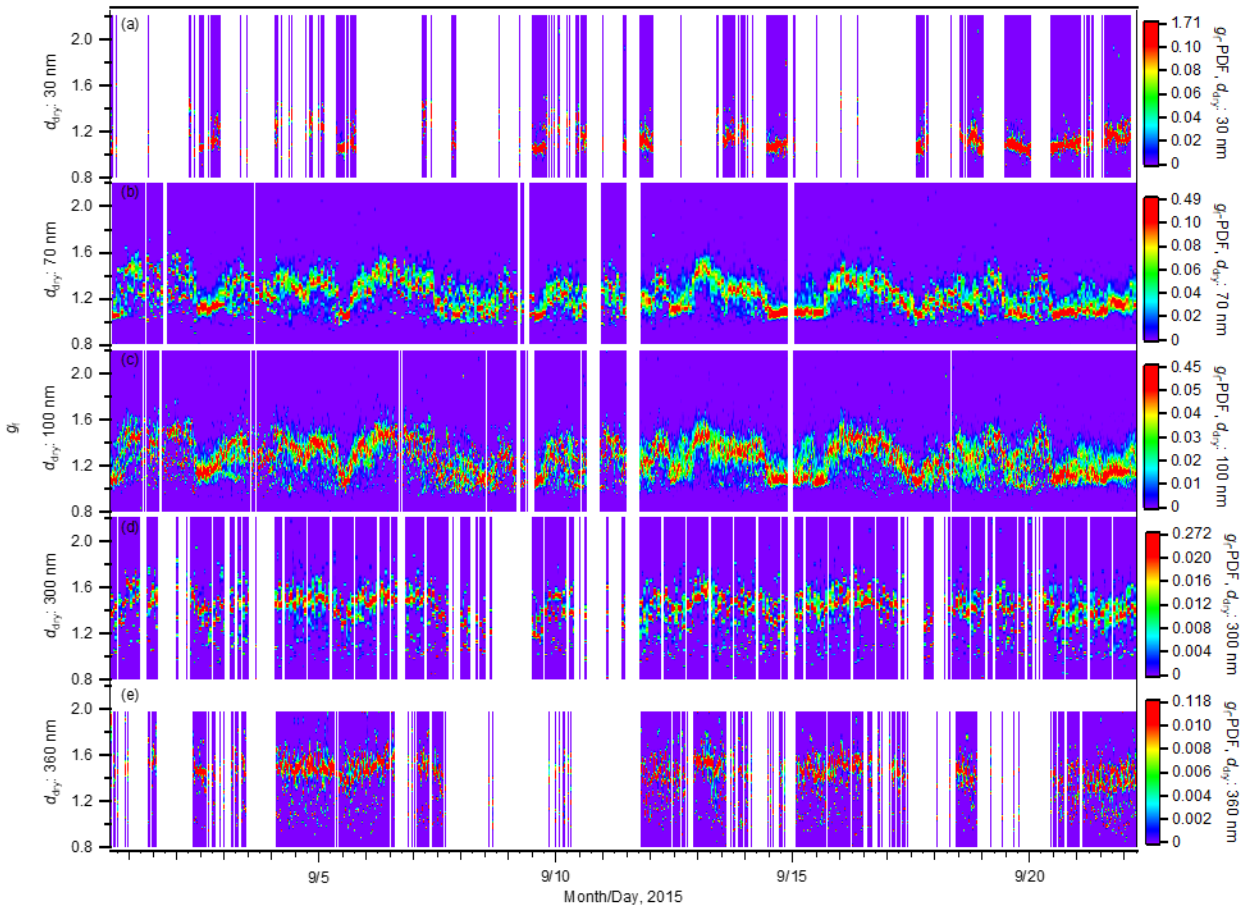

Figure S11: Time series of the probability distribution functions of the hygroscopic growth factors (g_f-PDF) of aerosol particles with d_{dry} of (a) 30, (b) 70, (c) 100, (d) 300, and (e) 360 nm.

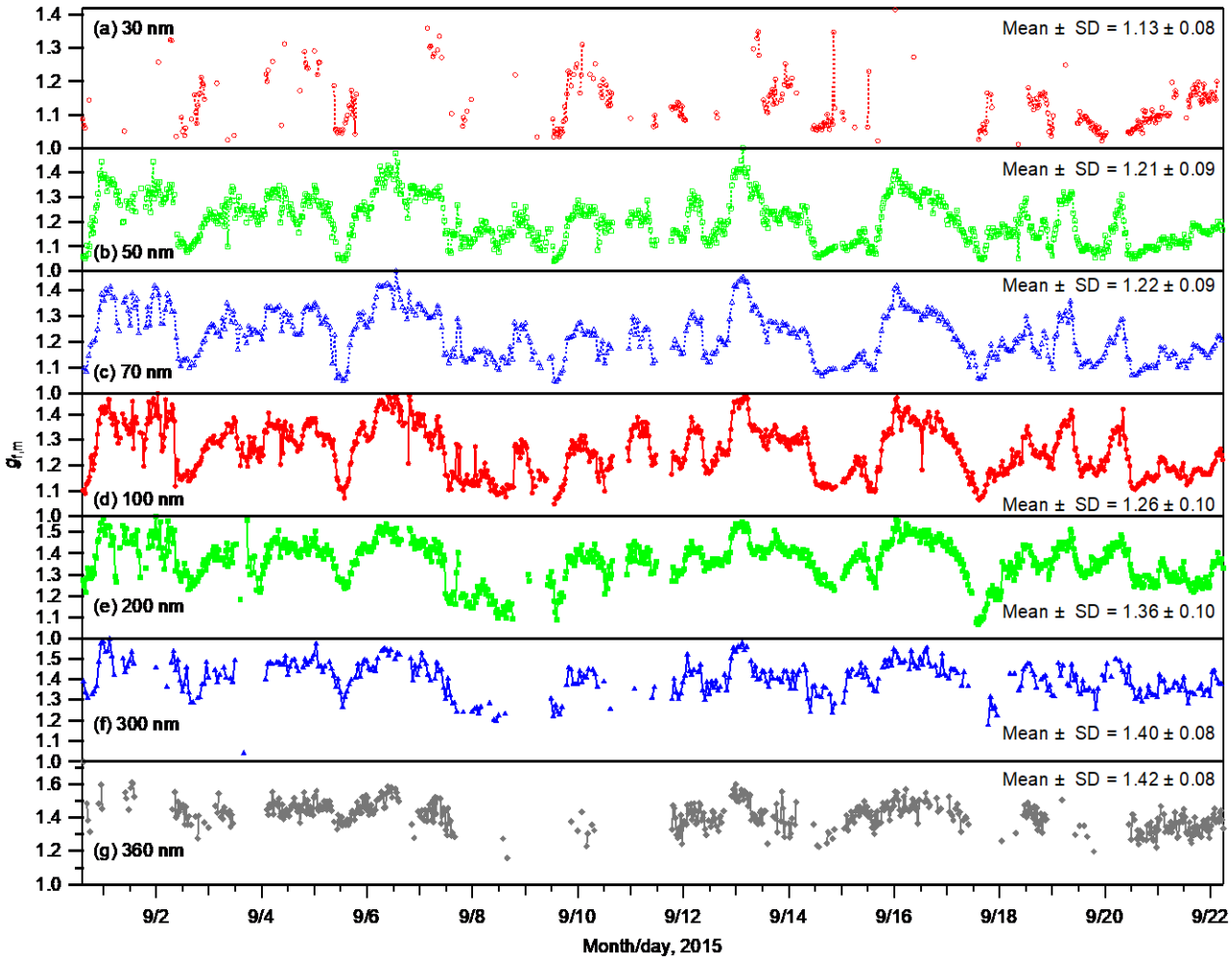

Figure S12: Time series of the mean growth factors ($g_{f,m}$) of aerosol particles with different dry diameters. The mean ± SD values over the entire study period for each diameter are also presented.

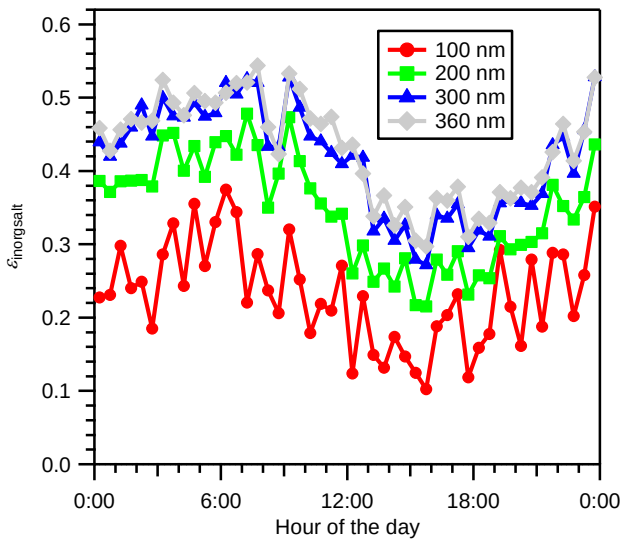

Figure S13: Diurnal variation of the size-resolved volume fractions of total inorganic salts ($\varepsilon_{inorgsalt}$) during the entire study period.

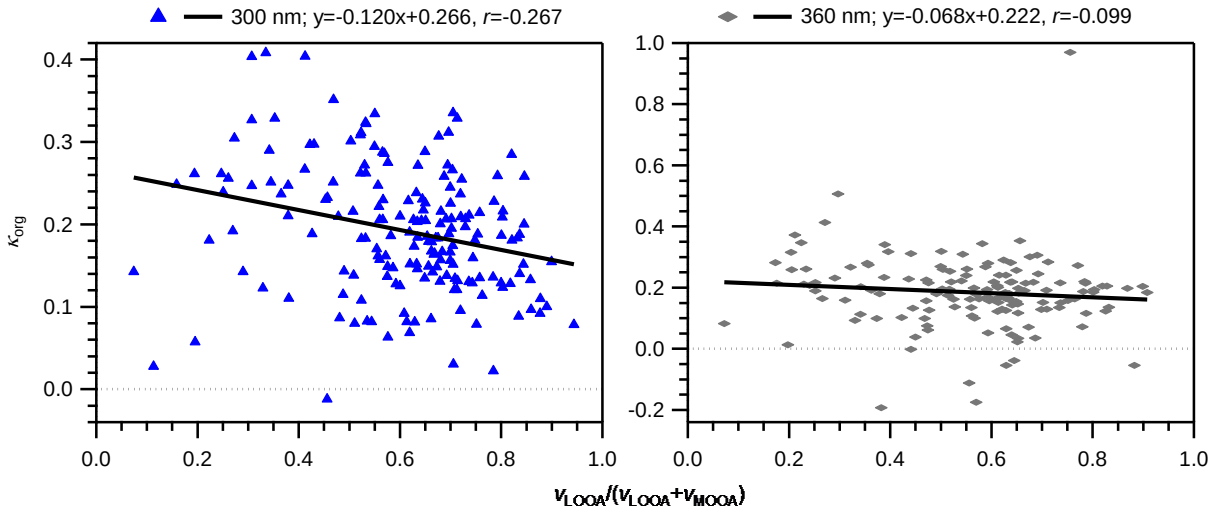

Figure S14: The κ_{org} versus $v_{LOOA}/(v_{LOOA}+v_{MOOA})$ for particles with d_{dry} of 300 and 360 nm. The time resolution of the data is 2 h. In each panel, marks and a solid line represent individual data and the corresponding linear regression line, respectively. The regression equation and correlation coefficient of each are also presented. Only data with ε_{org} greater than 0.40 are used.

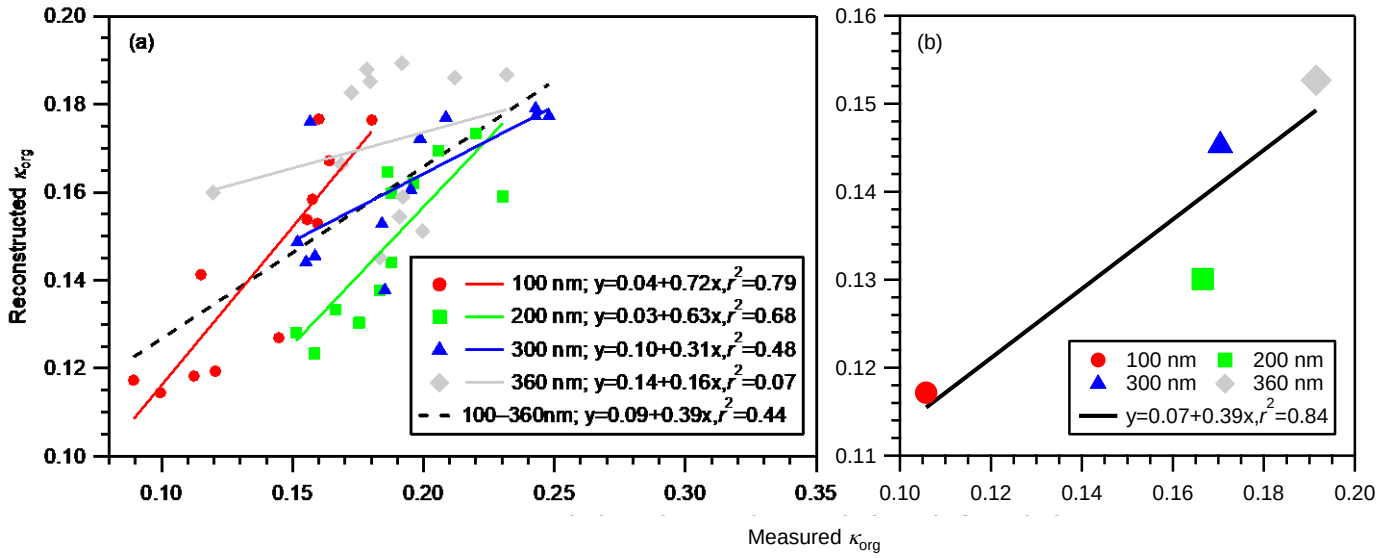

Figure S15: The κ_{org} reconstructed using κ_{LOOA}, κ_{MOOA}, and size-resolved $v_{LOOA}/(v_{LOOA}+v_{MOOA})$ (reconstructed κ_{org}) versus the κ_{org} derived from measured κ_t and aerosol chemical composition (measured κ_{org}; Sect. 3.2). In panel (a), markers represent size-resolved diurnal variation data at 2 h resolution, solid lines are linear regression lines for particles with respective diameters, and the dashed line is the linear regression line for all 100–360 nm particles. In panel (b), markers represent the size-resolved mean κ_{org} during 1200–2000 JST, and the solid line is the linear regression line for the size-resolved mean κ_{org}. Respective regression equations and coefficients of determination (r^2) are also presented. Only κ_{org} data with ε_{org} greater than 0.40 are used for the comparison.

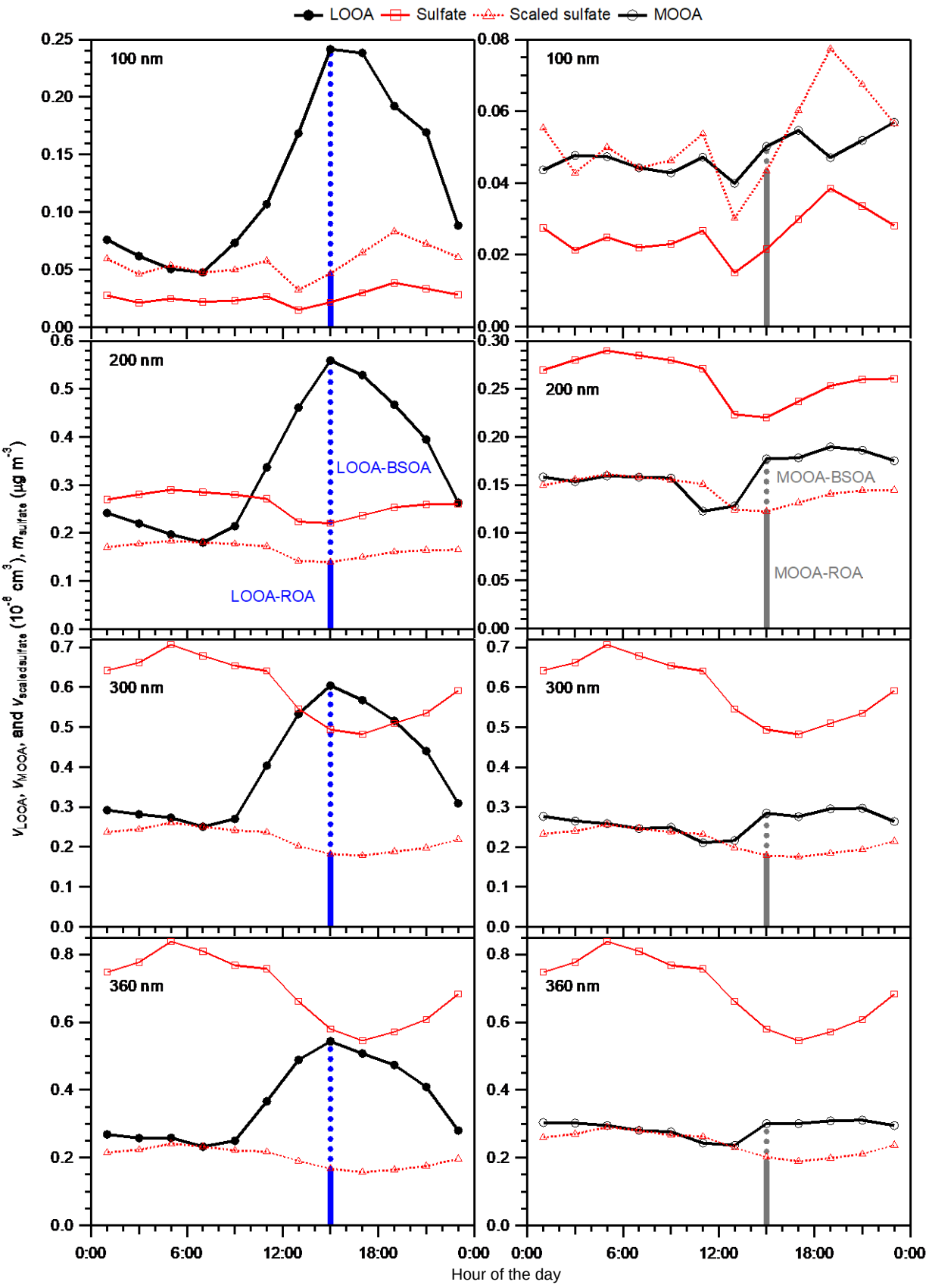
LOOA
Sulfate
Scaled sulfate
MOOA
100 nm
200 nm
300 nm
360 nm
LOOA-BSOA
LOOA-ROA
MOOA-BSOA
MOOA-ROA
v_{LOOA}, v_{MOOA}, and $v_{scaledsulfate}$ (10^{-8} cm^3), $m_{sulfate}$ (μg m^{-3})
Hour of the day
0:00
6:00
12:00
18:00

Figure S16: Diurnal variation of the volume concentrations of LOOA and MOOA and the mass concentration of sulfate for particles with d_{dry} of 100, 200, 300, and 360 nm over the entire study period. The scaled sulfate represents the diurnal variation of ROA that was contributed by LOOA (left panels) or MOOA (right panels). The scaling factor for the scaled sulfate in each panel is the mean volume concentration of OA during 0600–0800 JST, divided by the mean mass concentration of sulfate in the same period. The volume concentrations of LOOA and MOOA were derived from the respective mass concentrations (Text S8). The densities of LOOA and MOOA were calculated using their O:C and H:C ratios following Kuwata et al. (2012) and were 1.24 and 1.54 g cm^{-3}, respectively.

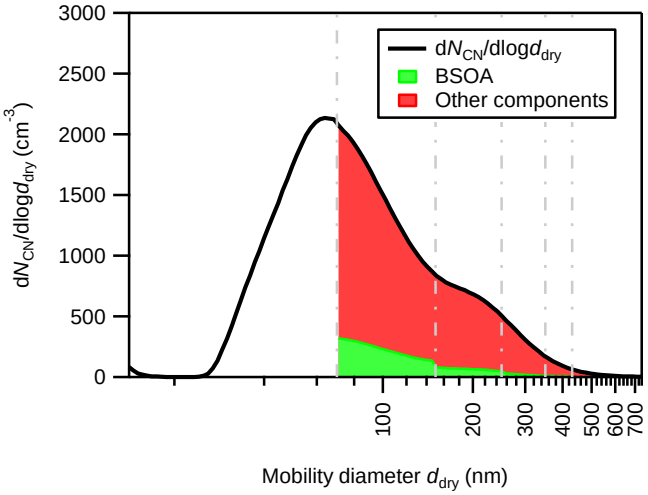

Figure S17: Estimate of the contributions of BSOA to the CCN number concentration. The solid line indicates the mean aerosol number-size distribution during the entire study period. Shaded areas in green represent the fraction of CCN contributed by BSOA and in red, that contributed by other components assuming a CCN activation diameter of 70 nm (Text S11).

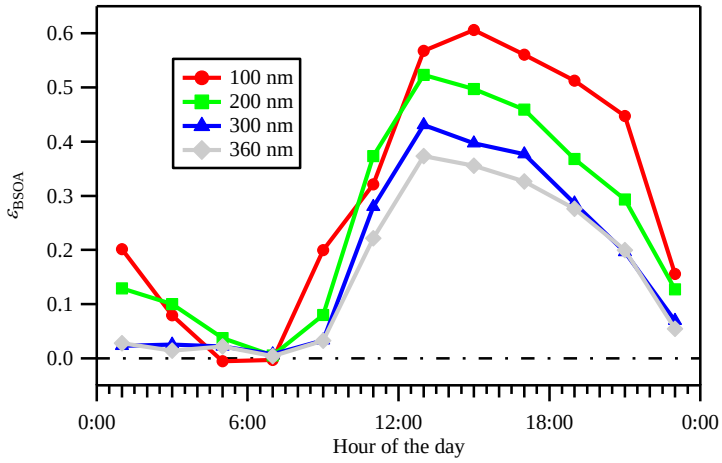

Figure S18: The diurnal variation of the volume fractions of BSOA (ε_{BSOA}) for particles with d_{dry} of 100, 200, 300, and 360 nm over the entire study period (Text S11).

Table S1: Mode diameters [a] of PSL size standards measured by DMAs in the HTDMA (DMA1 and DMA2) and the SMPS (DMA3) (mean ± SD, nm)

Manufacturer	DMA1		DMA2		DMA3	
warranty	Before [c]	After [d]	Before [c]	After [d]	Before [c]	After [d]
55 (± 1) [b]	56.6 ± 0.4	56.2 ± 0.4	56.8 ± 0.4	-	59.9 ± 0.2	-
100 (± 3) [b]	98.0 ± 0.2	98.4 ± 0.1	97.0 ± 0.1	96.2 ± 0.2	101.2 ± 0.3	101.1 ± 0.1
309 (± 9) [b]	297.7 ± 0.8	298.0 ± 0.4	290.4 ± 1.2	-	303.6 ± 0.3	-
498 (± 9) [b]	-	-	478.4 ± 5.8	-	499.6 ± 4.4	-

[a] The mean ± SD of the mode diameters from fittings are presented (unit: nm).
[b] Mean diameter (± the expanded uncertainty; $k = 2$).
[c] Before the atmospheric observations.
[d] After the atmospheric observations.

Table S2: The $g_{f,m}$ of ammonium sulfate (AS) particles measured under dry condition ($g_{f,m,dryAS}$) and at 85 % RH ($g_{f,m,wetAS}$), and calculated g_f of AS particles at 85 % RH ($g_{f,AS}$)

d_{dry} (nm)	30	50	70	100	200	300	360
$g_{f,m,dryAS}$	0.959	0.976	0.984	0.985	0.988	0.982	0.981
$g_{f,m,wetAS}$ [a]	1.52	1.54	1.54	1.54	1.55	1.57	1.59
$g_{f,AS}$ [a]	1.49	1.52	1.54	1.55	1.57	1.57	1.57
Difference (%) [b]	2.0	1.3	0	–0.65	–1.3	0	1.3

[a] Corrected for the difference of sizing between DMA1 and DMA2.
[b] $((g_{f,m,wetAS} - g_{f,AS}) / g_{f,AS}) \times 100$.

Table S3: The κ values of inorganic salts (κ_i) at 85 % RH derived using the surface tension of the solution and of pure water

	κ_i, with surface tension of solution				κ_i, with surface tension of pure water			
d_{dry} (nm)	100	200	300	360	100	200	300	360
AN	0.553	0.555	0.555	0.556	0.553	0.555	0.556	0.556
AS	0.533	0.527	0.525	0.524	0.531	0.526	0.524	0.524
LET	0.550	0.545	0.543	0.543	0.549	0.544	0.543	0.543
AHS	0.612	0.607	0.605	0.605	0.612	0.607	0.605	0.605
SA	0.972	0.959	0.955	0.953	0.971	0.959	0.955	0.953

Table S4: Data in Fig. 3 of the main manuscript ("DataInFigure3ofTheManuscript.xlsx").

Table S5: Data in Fig. 4 of the main manuscript ("DataInFigure4ofTheManuscript.xlsx").

Table S6: Data in Fig. 5 of the main manuscript ("DataInFigure5ofTheManuscript.xlsx")**.**

Table S7: Comparisons of κ_{org} and $v_{LOOA}/(v_{LOOA}+v_{MOOA})$ between particles with different d_{dry}

d_{dry} of particles to compare (nm)	1200–2000 JST				2000–1200 JST			
	κ_{org}		$v_{LOOA}/(v_{LOOA}+v_{MOOA})$		κ_{org}		$v_{LOOA}/(v_{LOOA}+v_{MOOA})$	
	Diff[a]	p-value[c]	Diff[b]	p-value[c]	Diff[a]	p-value[c]	Diff[b]	p-value[c]
200 vs 100	0.06	<0.01	–0.06	0.02	0.04	<0.01	–0.01	0.65
300 vs 200	<0.01	0.71	–0.08	<0.01	<0.01	0.31	–0.06	<0.01
360 vs 300	0.02	0.15	–0.04	<0.01	–0.02	0.02	–0.05	<0.01
360 vs 200	0.02	0.07	–0.11	<0.01	–0.02	0.07	–0.11	<0.01

[a] The mean of (the κ_{org} of particles with relatively large d_{dry} – the κ_{org} of particles with relatively small d_{dry}).
[b] The mean of (the $v_{LOOA}/(v_{LOOA}+v_{MOOA})$ of particles with relatively large d_{dry} – the $v_{LOOA}/(v_{LOOA}+v_{MOOA})$ of particles with relatively small d_{dry}).
[c] From 10 % two-sided t-test for the significance of the difference of Diff from zero. Low values indicate significant differences.

Table S8: Diurnal variation of κ_t and κ_{org} at 2 h resolution, and their mean and SD for the entire period

	κ_t							κ_{org}			
d_{dry} (nm)	30	50	70	100	200	300	360	100	200	300	360
0000–0200 JST	0.16	0.20	0.22	0.24	0.34	0.37	0.36	0.16	0.23	0.25	0.21
0200–0400 JST	0.22	0.21	0.22	0.24	0.34	0.37	0.35	0.16	0.20	0.21	0.18
0400–0600 JST	0.18	0.21	0.22	0.25	0.34	0.38	0.39	0.16	0.21	0.24	0.23
0600–0800 JST	0.21	0.22	0.21	0.25	0.35	0.38	0.36	0.18	0.22	0.24	0.19
0800–1000 JST	0.15	0.18	0.21	0.22	0.32	0.33	0.37	0.16	0.19	0.16	0.18
1000–1200 JST	0.13	0.16	0.16	0.19	0.29	0.33	0.34	0.12	0.17	0.15	0.12
1200–1400 JST	0.090	0.14	0.14	0.16	0.26	0.32	0.34	0.11	0.16	0.19	0.18
1400–1600 JST	0.083	0.13	0.13	0.16	0.24	0.28	0.33	0.10	0.15	0.16	0.20
1600–1800 JST	0.10	0.14	0.14	0.17	0.25	0.28	0.32	0.089	0.18	0.16	0.19
1800–2000 JST	0.13	0.15	0.16	0.19	0.27	0.31	0.32	0.12	0.18	0.18	0.19
2000–2200 JST	0.14	0.18	0.18	0.21	0.29	0.33	0.34	0.14	0.19	0.20	0.17
2200–0000 JST	0.12	0.19	0.20	0.23	0.31	0.35	0.36	0.16	0.19	0.20	0.17
Mean for entire period	0.12	0.18	0.18	0.21	0.30	0.34	0.35	0.13	0.18	0.19	0.19
SD for entire period	0.079	0.090	0.089	0.094	0.10	0.087	0.086	0.11	0.085	0.084	0.11

Table S9: Data in Fig. 6 of the main manuscript.

Hour of the day	$F_{CCN,OA}$ (%)	$F_{CCN,BSOA}$ (%; fresh BSOA)	$F_{CCN,BSOA}$ (%; aged BSOA)
0000–0200 JST	44.5	5.85	10.6
0200–0400 JST	44.9	2.66	4.89
0400–0600 JST	40.1	0.238	0.340
0600–0800 JST	42.8	-6.41×10^{-3}	−0.0374
0800–1000 JST	44.5	5.62	10.3
1000–1200 JST	42.7	12.7	21.3
1200–1400 JST	53.0	26.2	39.8
1400–1600 JST	52.7	28.4	42.7
1600–1800 JST	47.3	24.9	38.6
1800–2000 JST	45.7	19.8	31.9
2000–2200 JST	49.4	16.6	27.5
2200–0000 JST	45.3	4.99	9.11

Table S10: Different assumptions of κ_{org} for the prediction of $F_{CCN,OA}$

	TimeSize κ_{org}[a]				SizeReso κ_{org}[b]				TimeReso κ_{org}[c]				Single κ_{org}[d]			
d_{dry} (nm)	**100**	**200**	**300**	**360**	**100**	**200**	**300**	**360**	**100**	**200**	**300**	**360**	**100**	**200**	**300**	**360**
0000–0200 JST	0.16	0.23	0.25	0.21	0.14	0.19	0.19	0.19	0.21				0.18			
0200–0400 JST	0.16	0.20	0.21	0.18					0.19							
0400–0600 JST	0.16	0.21	0.24	0.23					0.21							
0600–0800 JST	0.18	0.22	0.24	0.19					0.21							
0800–1000 JST	0.16	0.19	0.16	0.18					0.17							
1000–1200 JST	0.12	0.17	0.15	0.12					0.14							
1200–1400 JST	0.11	0.16	0.19	0.18					0.16							
1400–1600 JST	0.10	0.15	0.16	0.20					0.15							
1600–1800 JST	0.089	0.18	0.16	0.19					0.15							
1800–2000 JST	0.12	0.18	0.18	0.19					0.17							
2000–2200 JST	0.14	0.19	0.20	0.17					0.17							
2200–0000 JST	0.16	0.19	0.20	0.17					0.18							

[a] Time- and size-resolved κ_{org}.
[b] Time-averaged, size-resolved κ_{org}.
[c] Time-resolved, size-averaged κ_{org}.
[d] Time- and size-averaged κ_{org}.

Table S11: Different assumptions of κ_{BSOA} for the prediction of $F_{CCN,BSOA}$

d_{dry} (nm)	Size-resolved κ_{BSOA}	Size-averaged κ_{BSOA}	Aged, size-resolved κ_{BSOA}
100	0.089	0.11	0.18
200	0.11		0.18
300	0.12		0.18
360	0.12		0.19

Table S12: Data in Fig. 7 of the main manuscript.

Hour of day	Ratios of different $F_{CCN,OA}$				Ratios of different $F_{CCN,BSOA}$		
	TimeSize κ_{org}[a]	SizeReso κ_{org}[b]	TimeReso κ_{org}[c]	Single κ_{org}[d]	Size-resolved κ_{BSOA}	Size-averaged κ_{BSOA}	Aged, Size-resolved κ_{BSOA}
0000–0200 JST	1	0.913	1.09	0.993	1	1.19	1.82
0200–0400 JST	1	0.932	1.04	1.01	1	1.17	1.84
0400–0600 JST	1	0.920	1.10	1.00	1	0.899	1.43
0600–0800 JST	1	0.876	1.04	0.951	1	3.61	5.83
0800–1000 JST	1	0.964	1.02	1.04	1	1.19	1.82
1000–1200 JST	1	1.10	1.05	1.18	1	1.14	1.68
1200–1400 JST	1	1.08	1.10	1.14	1	1.12	1.52
1400–1600 JST	1	1.13	1.13	1.19	1	1.13	1.50
1600–1800 JST	1	1.18	1.19	1.26	1	1.14	1.55
1800–2000 JST	1	1.06	1.13	1.15	1	1.15	1.61
2000–2200 JST	1	0.983	1.06	1.06	1	1.16	1.65
2200–0000 JST	1	0.950	1.04	1.03	1	1.18	1.82

[a] Time- and size-resolved κ_{org}.
[b] Time-averaged, size-resolved κ_{org}.
[c] Time-resolved, size-averaged κ_{org}.
[d] Time- and size-averaged κ_{org}.